Journal of Magnetic Resonance **140,** 91–107 (1999)
Article ID jmre.1999.1803, available online at http://www.idealibrary.com on IDEAL®

General Analysis of ^{14}N ($I = 1$) Electron Spin Echo Envelope Modulation

Hong-In Lee, Peter E. Doan, and Brian M. Hoffman[1]

Department of Chemistry, Northwestern University, Evanston, Illinois 60208

Received December 14, 1998; revised April 27, 1999

The analysis methods described to date for ^{14}N electron spin echo envelope modulation (ESEEM) mostly deal with isotropic g- and ^{14}N hyperfine coupling tensors. However, many cases of rhombic tensors are encountered. In the present report we present general equations for analyzing orientation-selective ESEEM and illustrate their use. (i) We present general equations for the nuclear interactions in an electron spin system where the EPR signal arises from an isolated Kramers doublet, then give the nuclear (electron-nuclear double resonance) frequencies for $I = 1$ associated with such a system. (ii) These are incorporated into equations for single-crystal ESEEM amplitudes, which in turn are incorporated into general equations for the orientation-selective ESEEM that arises when the EPR envelope of a frozen-solution (powder) sample is determined by g anisotropy. (iii) This development is first used in the simplest limit of an isotropic g-tensor and leads to a more general picture of the response of the $I = 1$ modulation amplitude to variations in the nuclear hyperfine and quadrupole coupling constants, relative to the nuclear Zeeman interaction, than had been presented previously. We find that strong modulation occurs not only in the well-known regime where the "exact/near cancellation" condition ($A/2 \sim \nu_N$) is satisfied, but also when the nuclear hyperfine interaction is much larger than the nuclear Zeeman interaction ($A/\nu_N > 3$) with $A/K = 4 \sim 5$. (iv) We then describe the orientation-selective ^{14}N ESEEM frequency-domain patterns (g vs frequency) in the presence of anisotropic (rhombic) hyperfine *and* electron Zeeman interactions for both coaxial and noncoaxial cases. We derive analytical solutions when the g-, hyperfine, and nuclear quadrupole tensors are coaxial. (v) The method is applied to the ESEEM of the nitrogenase MoFe protein (*Av*1) to determine the full hyperfine and nuclear quadrupole tensors of ^{14}N nuclei interacting with the $S = \frac{3}{2}$ FeMo-cofactor (Fe_7S_8Mo: homocitrate).

Key Words: **pulsed EPR; ESEEM; ^{14}N; electron spin echo envelope modulation; orientation-selective.**

INTRODUCTION

Characterization of the hyperfine and nuclear quadrupole coupling tensors for metallobiomolecules and free radicals through electron-nuclear double resonance (ENDOR) (*1*) and electron spin echo envelope modulation (ESEEM) (*2*) plays a vital role in chemistry and biochemistry. The observation of such interactions identifies the nuclei that make up an active site, and determination of the interaction tensors reveals details of its bonding and metrical structure. The methods for obtaining these nuclear interaction tensors from data collected with randomly oriented (powder, or frozen-solution) samples have been extensively developed for ENDOR (*1, 3–5*), but less so for ESEEM. This lack is of particular importance for analysis of the signals from a ^{14}N nucleus ($I = 1$) coupled to an electron spin, because nitrogen is one of the most extensively studied nuclei in ESEEM. At present there is no general treatment of ESEEM for a frozen-solution (powder) paramagnetic center whose EPR spectrum is determined by an anisotropic **g**-tensor, and which incorporates an $I = 1$ nucleus that experiences nuclear Zeeman and quadrupole interactions, as well as an anisotropic hyperfine coupling. An ESEEM (or ENDOR) spectrum collected at a fixed field is "orientation-selective" in that it results from only a well-defined subset of molecular (or **g**-tensor) orientations relative to the external magnetic field. Techniques have been described for extracting the full anisotropic nuclear hyperfine and quadrupole tensors from the 2D, ENDOR frequency vs field, pattern of ENDOR spectra collected at numerous fields across the EPR envelope (*1, 3–5*). In this report we apply the same approach to obtain the *general* equations for analyzing orientation-selective ESEEM and illustrate their use.

The background to the present report includes Mims' derivation of the complete density matrix of the electron spin echo modulation effect (*6, 7*), along with published methods for the analysis of ESEEM of $I = 1$ nuclei, with emphasis on isotropic **g**- and hyperfine tensors. Based on Muha's analytic solution to the problem of an $I = 1$ nucleus undergoing quadrupole interactions in an arbitrary magnetic field (*8, 9*), Astashkin *et al.* developed a qualitative analysis method in the frequency domain for ^{14}N ESEEM, but this is limited to weakly anisotropic hyperfine interactions (*10*). Flanagan and Singel illustrated the relationships between ESEEM peak amplitudes and the orientation of the external magnetic field relative to the nuclear quadrupole tensor frame for the case of isotropic hyperfine coupling (*11*). Effects of anisotropic hyperfine interac-

[1] To whom correspondence should be addressed. Fax: 847-491-7713. E-mail: bmh@nwu.edu.

1090-7807/99 $30.00

tions were examined in the frequency domain for orientationally disordered systems with an isotropic **g**-tensor by Reijerse and Keijers (*12*). More recently, analytical solutions were described for cases of weak nuclear quadrupole coupling, such as ^{2}H (*13*). However, this treatment is not suitable for ^{14}N where the nuclear quadrupole coupling is strong compared to the nuclear Zeeman and the hyperfine interactions.

Some orientation-selective ^{1}H and ^{2}H ESEEM experiments have been reported (*14–17*), but only a few cases have been published for ^{14}N ESEEM. Flanagan *et al.* constructed the magnetic field profile of the amplitude ratios of two-pulse ^{14}N ESEEM peaks across the EPR absorption envelope of mercaptoethanol complex of low spin Fe(III) myoglobin to determine the orientation of the ^{14}N nuclear quadrupole tensor axis of the proximal imidazole ring with respect to **g**-tensor axis (*18*). Also, van Dam *et al.* applied the same approach to derive the ^{14}N tensor components of the remote nitrogen in Cu-imidazole systems (*19*). *But* these reports in fact relied on a nearly isotropic hyperfine coupling. Analytical solutions at $g_{\parallel}$ and $g_{\perp}$ positions for oxovanadium complexes were derived to extract ^{14}N tensors (*20, 21*). Here, the ^{14}N hyperfine couplings are largely isotropic and the anisotropic interaction was treated as a perturbation.

In the present paper, we develop for the first time a systematic approach that permits the determination of ^{14}N tensors for systems where **g**- and the hyperfine tensors are dominated by anisotropic (rhombic) interactions, and thus where the earlier methods are not applicable. To do that, (i) we present general equations for the nuclear interactions in an electron-spin system where the EPR signal arises from an isolated Kramers doublet, then give the nuclear (ENDOR) frequencies for $I = 1$ associated with such a system. (ii) These are incorporated into equations for single-crystal ESEEM amplitudes, which in turn are incorporated into general equations for the orientation-selective ESEEM that arises when the EPR envelope of a frozen-solution (powder) sample is determined by g anisotropy. (iii) This development is first used in the simplest limit of an isotropic **g**-tensor to examine how the $I = 1$ modulation amplitudes respond as the nuclear hyperfine and quadrupole coupling constants are varied relative to the nuclear Zeeman interaction, thereby allowing us to draw a more general picture of the behavior of the modulation amplitude than has been presented previously. We find that strong net modulation occurs not only in the well-known regime where the "exact/near cancellation" condition is satisfied, but also when the nuclear hyperfine interaction is much larger than the nuclear Zeeman interaction and the nuclear quadrupole coupling constant is comparable to the hyperfine coupling constant. (iv) We then describe the orientation-selective ^{14}N ESEEM frequency-domain patterns (g vs frequency) in the presence of anisotropic (rhombic) hyperfine *and* electron Zeeman interactions for both coaxial and noncoaxial cases. We derive analytical solutions when the **g**-, hyperfine, and nuclear quadrupole tensors are coaxial. (v) The method is applied to the ESEEM of the nitrogenase MoFe protein (*Av*1) to determine the full hyperfine and nuclear quadrupole tensors of ^{14}N nuclei interacting with the $S = \frac{3}{2}$ FeMo-cofactor (Fe_7S_8Mo: homocitrate) (*22, 23*).

THEORY AND APPLICATION

(i-a). Nuclear interactions for $S = \frac{1}{2}$. When an electron spin of $S = \frac{1}{2}$ coupled to a nucleus of spin $I > \frac{1}{2}$ is placed in an external magnetic field, $\mathbf{H}_o$, the total magnetic interaction of the system is described by a Hamiltonian that includes the electron Zeeman interaction ($\mathcal{H}_e$), the nuclear Zeeman and hyperfine couplings ($\mathcal{H}_{int}$), and the nuclear quadrupole coupling ($\mathcal{H}_q$) (*1, 24, 25*).

$$\mathcal{H} = \mathcal{H}_e + \mathcal{H}_{int} + \mathcal{H}_q \quad [1]$$

where

$$\mathcal{H}_e = \beta_e \mathbf{S} \cdot \mathbf{g} \cdot \mathbf{H}_o, \quad [2]$$

$$\mathcal{H}_{int} = -g_N \beta_N \mathbf{I} \cdot \mathbf{H}_o + h\mathbf{I} \cdot \mathbf{A} \cdot \mathbf{S}, \quad [3]$$

and

$$\mathcal{H}_q = h\mathbf{I} \cdot \mathbf{P} \cdot \mathbf{I}. \quad [4]$$

Here β_e, $\mathbf{g}$, g_N, β_N, h, $\mathbf{A}$, and $\mathbf{P}$ are the Bohr magneton, the electron **g**-tensor, the nuclear g-value, the nuclear magneton, Planck's constant, the hyperfine coupling tensor, and the nuclear quadrupole coupling tensor, respectively; each interaction matrix ($\mathbf{g}$, $\mathbf{A}$, $\mathbf{P}$) is diagonal in its own reference frame. For the relatively small nuclear interactions of interest here, compared to the electron Zeeman interaction (high field approximation, $\nu_e = g_e\beta_e H_o/h \gg A, P$, $\nu_N = g_N\beta_N H_o/h$), there is no loss in ignoring off-diagonal matrix elements in the electron spin. In this case, the nuclear spin Hamiltonian governing ESEEM and ENDOR frequencies within the individual electron-spin manifolds, $m_s = \pm\frac{1}{2}$, is described by the sum of the nuclear Zeeman, hyperfine, and nuclear quadrupole interactions,

$$\mathcal{H}_{N\pm} = \mathcal{H}_{int\pm} + \mathcal{H}_{q\pm}. \quad [5]$$

The first step in deriving ESEEM/ENDOR frequencies begins with the expression of the nuclear Zeeman and hyperfine interactions in the electron **g**-tensor frame (*1*),

$$\mathcal{H}_{int\pm} = h\mathbf{I} \cdot [(\pm 1/2)\,{}^{g}\mathbf{A} \cdot \mathbf{g}/g_{eff} - \nu_N] \cdot \boldsymbol{l} \equiv h\mathbf{I} \cdot \Gamma_{\pm} \quad [6]$$

where

$$\Gamma_{i\pm} = \frac{(\pm 1/2)}{g_{\text{eff}}} \sum_{j=1}^{3} g_j l_j^{\text{g}} A_{ij} - \nu_{\text{N}} l_i \quad \text{for } i = 1, 2, 3. \quad [7]$$

Here, $^{\text{g}}\mathbf{A}$ and is the hyperfine tensor matrix transformed into the **g**-tensor frame by a rotation matrix $\mathbf{M}(\alpha, \beta, \gamma)$ which is defined as the matrix that rotates **g** into the **A** frame ($^{\text{g}}\mathbf{A} = \mathbf{M}^{-1} \cdot \mathbf{A} \cdot \mathbf{M}$) (*26, 27*); g_{eff} is the experimental g-value of observation; ν_{N} the nuclear Larmor frequency ($\nu_{\text{N}} = g_{\text{N}}\beta_{\text{N}}H_{\text{o}}/h$); and $\boldsymbol{l}$ is a unit vector along $\mathbf{H}_{\text{o}}$, written as direction-cosines with respect to the **g**-frame.

(i-b). Nuclear interactions for $S' = \frac{1}{2}$. The above treatment can be readily generalized to the case of a half-integer electron-spin system, $S > \frac{1}{2}$ where the EPR signal comes from an isolated Kramers doublet, and can be treated in terms of a fictitious spin, $S' = \frac{1}{2}$ with Zeeman interaction given by (*24*).

$$\mathcal{H}_{\text{e}} = \beta_{\text{e}} \mathbf{S}' \cdot \mathbf{g}' \cdot \mathbf{H}_{\text{o}}. \quad [8]$$

The principal values of the **g′**-tensor are determined by the details of the electron-spin system and could be taken as inputs for the treatment presented here. For concreteness, we here illustrate the approach with the specific case of $S = \frac{3}{2}$, which applies to the nitrogenase MoFe protein (*Av*1), whose resting state exhibits an $S = \frac{3}{2}$ EPR signal arising from the FeMo-cofactor cluster (*28*).

A high-spin EPR spectrum can be described by the Hamiltonians of the zero-field splitting ($\mathcal{H}_{\text{zfs}}$) and the electron Zeeman interaction ($\mathcal{H}_{\text{e}}$) as (*24*)

$$\begin{aligned}\mathcal{H} &= \mathcal{H}_{\text{zfs}} + \mathcal{H}_{\text{e}} \\ &= [D(\mathbf{S}_z^2 - S(S+1)/3) + E(\mathbf{S}_x^2 - \mathbf{S}_y^2)] \\ &\quad + \beta_{\text{e}} \mathbf{S} \cdot \mathbf{g} \cdot \mathbf{H}_{\text{o}}. \end{aligned} \quad [9]$$

Here, D and E are the axial and rhombic zero-field splitting parameters and the rhombicity is measured by $\lambda = E/D \leq \frac{1}{3}$; **g** is the **g**-tensor describing the Zeeman interaction and the other symbols have the usual meaning. For $S = \frac{3}{2}$ spin state, two Kramers doublets are separated by $\Delta = 2D(1 + 3\lambda^2)^{1/2}$ in zero magnetic field. Since the separation, $D = 12.2\ \text{cm}^{-1}$ for nitrogenase *Av*1 is large compared both to $k_{\text{B}}T$ at experimental liquid-helium temperature and to the electron Zeeman interaction at 9 GHz, the EPR spectrum of *Av*1 represents the transitions only in the lower, $m_s = \pm\frac{1}{2}$ doublet (*29*). As a result it can be represented by a fictitious spin $S' = \frac{1}{2}$ characterized by a **g′**-tensor that is coaxial with the fine-structure interaction (Eq. [8]), with

$$g'_z = g_{\parallel} \quad [10]$$

$$g'_{x,y} = g_{\perp}[1 + (1 \pm 3|\lambda|)/(1 + 3\lambda^2)^{1/2}]. \quad [11]$$

For *Av*1, the experimentally measured principal values, $g'_{x,y,z} = (4.33, 3.77, 2.01)$ correspond to a $S = \frac{3}{2}$ representation where $g_{\parallel} = 2.01$, $g_{\perp} = 2.005$, and $|\lambda| = 0.053$.

The nuclear quadrupole interaction is independent of electron spin and is unchanged, compared to $S = \frac{1}{2}$. The hyperfine Hamiltonian can be transformed to the fictitious spin by the Wigner–Eckart theorem (*24*),

$$\begin{aligned}\mathcal{H}_{\text{hf}} &= h\mathbf{I} \cdot {}^{\text{g}}\mathbf{A} \cdot \mathbf{S} = h\Sigma\, {}^{\text{g}}A_{ij} I_i S_j \\ &= h\mathbf{I} \cdot \mathbf{A}' \cdot \mathbf{S}' = h\Sigma A'_{ij} I_i S'_j \quad (A'_{ij} = {}^{\text{g}}A_{ij} g'_j/g_j) \\ &= h\mathbf{I} \cdot ({}^{\text{g}}\mathbf{A} \cdot \hat{g}') \cdot \mathbf{S}' \quad (\hat{g}'_{ij} = \delta_{ij} g'_j/g_j). \end{aligned} \quad [12]$$

Here, $^{\text{g}}\mathbf{A}$ is the hyperfine tensor transformed into **g′**-tensor reference frame. Note that the transformation to **A′** introduces anisotropic behavior into the hyperfine interaction even if the intrinsic coupling is isotropic. For example, an intrinsically isotropic coupling constant of 1.00 MHz would result in a measured hyperfine tensor, **A′**, that would be anisotropic with principal value of **A′** = [2.15, 1.90, 1.00] MHz corresponding to **g′** = [4.3, 3.8, 2.0].

For an $S = \frac{1}{2}$ system, the nuclear Zeeman interaction can usually be taken as a scalar coupling, $\mathcal{H}_{\text{nz}} = -g_{\text{N}}\beta_{\text{N}}\mathbf{I} \cdot \mathbf{H}_{\text{o}}$. However, the low-lying $m_s = \pm\frac{1}{2}$ doublet of a high-spin system can experience a large, anisotropic pseudonuclear Zeeman effect (*24*) caused by field-induced coupling to the high-lying doublet. Hence, the nuclear Zeeman interaction is described by an effective nuclear $\mathbf{g}^{\text{N}}$-tensor coincident with the zero-field splitting tensor axis (**g′**-tensor),

$$\mathcal{H}_{\text{nz}} = -\beta_{\text{N}} \mathbf{I} \cdot \mathbf{g}^{\text{N}} \cdot \mathbf{H}_{\text{o}}, \quad [13]$$

where for nitrogenase ($S = \frac{3}{2}$)

$$g_{ij}^{\text{N}} = g_{\text{N}}[\delta_{ij} + 3/2(g_{\text{e}}\beta_{\text{e}}/g_{\text{N}}\beta_{\text{N}})({}^{\text{g}}A_{ij}/\Delta)(1 - \delta_{iz})] \quad [14]$$

under the simplification of setting $\lambda = 0$. The sum of the nuclear hyperfine and Zeeman Hamiltonian for $S' = \frac{1}{2}$ is then

$$\mathcal{H}_{\text{int}\pm} = h\mathbf{I} \cdot \mathbf{A}' \cdot \mathbf{S}' - \beta_{\text{N}} \mathbf{I} \cdot \mathbf{g}^{\text{N}} \cdot \mathbf{H}_{\text{o}} \equiv h\mathbf{I} \cdot \Gamma_{\pm} \quad [15]$$

where, for nitrogenase in particular,

$$\Gamma_{i\pm} = \frac{(\pm 1/2)}{g'_{\text{eff}}} \sum_{j=1}^{3} l_j \times \left[g'_j A'_{ij} - \nu_N \left(\delta_{ij} + \frac{3 g_e \beta_e A'_{ij} (1 - \delta_{iz})}{2 g_N \beta_N \Delta} \right) \right], \quad \text{for } i = 1, 2, 3 \text{ (or } x, y, z). \tag{16}$$

(i-c). ^{14}N modulation frequencies and amplitudes. If we define the rotation matrix, Ξ, that rotates the **g**-frame into the nuclear quadrupole frame, the vector, $\mathbf{\Gamma}_{\pm}$, can be reexpressed in the nuclear quadrupole axis system, and the nuclear Hamiltonian becomes

$$\mathcal{H}_{\text{int}\pm} = h \mathbf{I} \cdot \Lambda_{\pm}, \tag{17}$$

where

$$\Lambda_{\pm} \equiv \Xi^{-1} \cdot \Gamma_{\pm}. \tag{18}$$

The overall nuclear Hamiltonian operator describing ESEEM, expressed in the nuclear quadrupole axis system, then is given by

$$\mathcal{H}_{N\pm} = h \mathbf{I} \cdot \Lambda_{\pm} + h \mathbf{I} \cdot \mathbf{P} \cdot \mathbf{I} \tag{19}$$

$$= h[\Lambda_{1\pm} \mathbf{I}_X + \Lambda_{2\pm} \mathbf{I}_Y + \Lambda_{3\pm} \mathbf{I}_Z + K(1 - \eta) \mathbf{I}_X^2 + K(1 + \eta) \mathbf{I}_Y^2 - 2K \mathbf{I}_Z^2], \tag{20}$$

where $K = e^2 qQ/4$ and η is the asymmetry parameter. This leads to the Hamiltonian matrix (*25*),

$$\underline{\boldsymbol{H}}_{N\pm} = h \begin{bmatrix} K(1 - \eta) & \Lambda_{3\pm} & i\Lambda_{2\pm} \\ \Lambda_{3\pm} & K(1 + \eta) & \Lambda_{1\pm} \\ -i\Lambda_{2\pm} & \Lambda_{1\pm} & -2K \end{bmatrix} \tag{21}$$

in the basis, $|T_X\rangle$, $|T_Y\rangle$, and $|T_Z\rangle$, the pure nuclear quadrupole eigenstates. Muha has provided the exact eigenvalues ($h\nu_{\pm}$) and eigenvectors ($\Phi_{k\pm}$) of the matrix (Eq. [21]) (*8, 9, 25*):

$$\nu_{k\pm} = (\tfrac{4}{3}|p_{\pm}|)^{1/2} \cos[(\beta_{\pm} + 2\pi k)/3], \text{ for } k = 0, 1, 2, \tag{22}$$

$$\Phi_{k\pm} = N_{\pm} \begin{bmatrix} \Lambda_{1\pm}\Lambda_{3\pm} - i\Lambda_{2\pm} V_{k\pm} \\ \Lambda_{1\pm} U_{k\pm} - i\Lambda_{2\pm}\Lambda_{3\pm} \\ -\Lambda_{3\pm}^2 + V_{k\pm} U_{k\pm} \end{bmatrix}, \tag{23}$$

where $N_{\pm}$ is the normalization factor,

$$\beta_{\pm} = \cos^{-1}[(3/|p_{\pm}|)^{3/2} (q_{\pm}/2)], \tag{24}$$

$$p_{\pm} = -[K^2(3 + \eta^2) + \Lambda_{1\pm}^2 + \Lambda_{2\pm}^2 + \Lambda_{3\pm}^2], \tag{25}$$

$$q_{\pm} = -K[2K^2(1 - \eta^2) + (1 - \eta)\Lambda_{1\pm}^2 + (1 + \eta)\Lambda_{2\pm}^2 - 2\Lambda_{3\pm}^2], \tag{26}$$

$$V_{k\pm} = [K(1 + \eta) - \nu_{k\pm}], \tag{27}$$

and

$$U_{k\pm} = [K(1 - \eta) - \nu_{k\pm}]. \tag{28}$$

The nuclear transition frequencies observed by ESEEM/ENDOR are then straightforwardly written as (*9*)

$$\nu_{n\pm} = \nu_{k\pm} - \nu_{k'\pm} = \left(\frac{4}{|p_{\pm}|} \right)^{1/2} \cos[(\beta_{\pm} + n\pi)/3] \quad n = k + k' = 1, 2, 3(k' < k). \tag{29}$$

Assuming δ-function EPR and ESEEM linewidths, then for a single molecular orientation the two-pulse ESEEM intensities (modulation depths) at the fundamental nuclear transition frequencies are (*6, 7*)

$$I^{(2)}_{\nu(n+)} = \tfrac{2}{3} \sum_{i=0}^{2} |\Phi^+_{k+} \cdot \Phi_{i-}|^2 |\Phi^+_{k'+} \cdot \Phi_{i-}|^2, \tag{30}$$

$$I^{(2)}_{\nu(m-)} = \tfrac{2}{3} \sum_{i=0}^{2} |\Phi^+_{i+} \cdot \Phi_{l-}|^2 |\Phi^+_{i+} \cdot \Phi_{l'-}|^2, \tag{31}$$

$$n = k + k' = 1, 2, 3(k' < k); \quad m = l + l' = 1, 2, 3(l' < l); \; k, k', l, l' = 0, 1, 2.$$

The combination (sum or difference) frequencies can be described, but are not discussed here. The corresponding intensities in three-pulse ESEEM are (*6, 7*)

$$I^{(3)}_{\nu(n+)} = \tfrac{1}{3} \sum_{i=0}^{2} |\Phi^+_{k+} \cdot \Phi_{i-}|^2 |\Phi^+_{k'+} \cdot \Phi_{i-}|^2 + \tfrac{2}{3} \sum_{m=1}^{3} \text{Re}[(\Phi^+_{k+} \cdot \Phi_{l-})^* (\Phi^+_{k+} \cdot \Phi_{l'-}) \times (\Phi^+_{k'+} \cdot \Phi_{l'-})^* (\Phi^+_{k'+} \cdot \Phi_{l-})] \cos(2\pi \nu_{m-} \tau), \tag{32}$$

$$I^{(3)}_{\nu(m-)} = \tfrac{1}{3} \sum_{i=0}^{2} |\Phi^+_{i+} \cdot \Phi_{l-}|^2 |\Phi^+_{i+} \cdot \Phi_{l'-}|^2 + \tfrac{2}{3} \sum_{n=1}^{3} \text{Re}[(\Phi^+_{k+} \cdot \Phi_{l-})^* (\Phi^+_{k+} \cdot \Phi_{l'-}) \times (\Phi^+_{k'+} \cdot \Phi_{l'-})^* (\Phi^+_{k'+} \cdot \Phi_{l-})] \cos(2\pi \nu_{n+} \tau), \tag{33}$$

$$n = k + k' = 1, 2, 3(k' < k); \quad m = l + l' = 1, 2, 3(l' < l); \; k, k', l, l' = 0, 1, 2.$$

(ii). Expressions for orientation-selective ESEEM. The previous equations present ESEEM/ENDOR frequencies (Eq. [29]) and ESEEM intensities (Eqs. [30]–[33]) for a single orientation. An orientation-selective ESEEM signal obtained at a given g-value from a powder sample whose EPR envelope is determined by g-anisotropy arises from the well-defined subset of molecular orientations associated with the curve, s_g, that satisfy $g^2 = g^2(\theta, \phi) = g_x^2\sin^2\theta\cos^2\phi + g_y^2\sin^2\theta\sin^2\phi + g_z^2\cos^2\theta$, where θ and ϕ represent the orientation of the external magnetic field with respect to the **g**-tensor frame. If one takes a δ-function component EPR linewidth, $\delta(g' - g)$, such an orientation-selective, frequency-domain ESEEM spectrum can be expressed as a sum of convolutions over the ESEEM/ENDOR frequencies that arise on the curve s_g (*1, 4*),

$$I(\nu, g) = \frac{1}{4\pi}\sum_n\sum_{\pm}\int_{s_g} L(\nu - \nu_{n\pm})I_{\nu(n\pm)}\delta(g' - g)d\sigma, \quad [34]$$

where $L(x)$ is an ESEEM lineshape function and $I_{\nu(n\pm)}$ are the two- or three-pulse intensities (Eqs. [30]–[33]). The factor of $4\pi(=\int d\sigma)$ normalizes the equation. The area element associated with an orientation (ϕ, g) is (*1*)

$$d\sigma = \left(\frac{g}{g^2 - g_z^2}\right)\frac{\sin^2\theta(\phi, g)}{\cos\theta(\phi, g)}\,d\phi dg \equiv w(\phi, g)d\phi dg, \quad [35]$$

and thus Eq. [34] for the ESEEM intensity at a given g-value can be rewritten as

$$I(\nu, g) = \frac{1}{4\pi}\sum_n\sum_{\pm}\int_{s_g} L(\nu - \nu_{n\pm})I_{\nu(n\pm)}w(\phi, g)d\phi. \quad [36]$$

Note that this approach leads to the orientation-selective intensity being expressed as single integral along the curve, s_g, rather than a double integral over the sphere (Euler angles, θ and ϕ). When one takes into account a nonzero EPR linewidth, the ESEEM intensity becomes

$$I(\nu, g) = \frac{1}{4\pi}\sum_n\sum_{\pm}\int\int_{s_{g'}} L(\nu - \nu_{n\pm})I_{\nu(n\pm)} \times w(\phi, g')R(g - g')d\phi dg', \quad [37]$$

where $R(x)$ is the component EPR lineshape function.

(iii). Isotropic g- and hyperfine tensors. We first apply these equations to reexamine the simplified situation of isotropic **g**- and hyperfine tensors. The methods of analyzing ^{14}N ESEEM for this case have been developed extensively (*10, 11*). However, our new approach discloses a new regime which exhibits strong modulation, in addition to the well-known exact/near cancellation regime. We first describe the traditional method as background, then present our approach.

In the case of isotropic **g**- and hyperfine tensors, there is no orientation selection: all orientations contribute to the ESEEM spectrum. The nuclear spin Hamiltonian describing the ESEEM is obtained simply, by substituting $\Lambda_{\pm} = (A/2 \pm \nu_n)\boldsymbol{l}$ in Eq. [19]. Here, A is the isotropic hyperfine coupling constant and $\boldsymbol{l}$ is the unit vector along the magnetic field, expressed with respect to the nuclear quadrupole frame. Using Muha's solution, Astashkin *et al.* developed a graphical method to find the nuclear transition frequencies, ν, as the solution(s) of the equation, $F(x) = f(\theta, \phi)$ (*8–10*), where

$$F(x) = \{2(1 - \eta^2) \pm 3^{-3/2}[x^2 - w^2 - 3 - \eta^2] \times [4w^2 + 4(3 + \eta^2) - x^2]^{1/2}\}/w^2, \quad [38]$$

$$f(\theta, \phi) = (3 - \eta\cos 2\phi)\cos^2\theta + \eta\cos 2\phi - 1, \quad [39]$$

$$w = (A/2 \pm \nu_n)/K, \quad [40]$$

and

$$x = \nu/K. \quad [41]$$

Here, θ and ϕ represent the orientation of the external magnetic field with respect to the nuclear quadrupole axis system. This method, which had been used previously in the study of electron triplet states (*30*), is convenient for qualitative predictions of a ^{14}N ESEEM pattern. Many systems studied by ^{14}N ESEEM show $w < 1$ in one electron-spin manifold, but $w > 1$ in the other (*2, 11*). In an electron-spin manifold with $w < 1$, the nuclear Zeeman and hyperfine interactions are opposed and largely cancel, so that the nuclear states are mostly determined by the nuclear quadrupole coupling. All three nuclear transition lines from this manifold usually have narrow peaks because the frequencies are dominated by the nuclear quadrupole interaction and are largely independent of the orientation of the magnetic field. In contrast, the nuclear Zeeman and the hyperfine interactions are dominant in an electron-spin manifold with $w > 1$, so that the nuclear states are mostly nuclear spin-projection (m_I) states. In this manifold, the single-quantum transitions ($\Delta m_I = \pm 1$) are dependent on the orientation of the magnetic field and a powder ESEEM spectrum, which is the sum of the transitions from all orientations of a randomly distributed sample, is broad and hard to observe. The double-quantum transition (dq, $\Delta m_I = \pm 2$), however, is only weakly dependent on orientation even for this manifold, and the dq transition thus is narrow and readily detected. Because the electron-spin echo is modulated with the nuclear frequencies from both electron-spin manifolds ($m_s = \pm\frac{1}{2}$),

^{14}N ESEEM commonly shows a four-line pattern (ν_0, ν_-, ν_+, dq) when $w_- < 1$, $w_+ > 1$; instead a two-line pattern (dq$_+$, dq$_-$) arises when w_-, $w_+ > 1$. We ignore cases of small nuclear interaction, w_-, $w_+ < 1$, because they give very small modulation.

For isotropic **g**- and nuclear hyperfine tensors, the dependence of the intensities and nuclear transition frequencies on the hyperfine and the nuclear quadrupole couplings can be conveniently studied by reformulating the Hamiltonian matrix (Eq. [21]) as

$$\underline{H}_{N\pm} = hK \begin{bmatrix} 1-\eta & \bar{\nu}\left(\pm\frac{\bar{A}}{2}-1\right)\cos\theta & i\bar{\nu}\left(\pm\frac{\bar{A}}{2}-1\right)\sin\theta\sin\phi \\ \bar{\nu}\left(\pm\frac{\bar{A}}{2}-1\right)\cos\theta & 1+\eta & \bar{\nu}\left(\pm\frac{\bar{A}}{2}-1\right)\sin\theta\cos\phi \\ -i\bar{\nu}\left(\pm\frac{\bar{A}}{2}-1\right)\sin\theta\sin\phi & \bar{\nu}\left(\pm\frac{\bar{A}}{2}-1\right)\sin\theta\cos\phi & -2 \end{bmatrix}, \quad [42]$$

$$\bar{\nu} = \nu_N/K, \text{ and } \bar{A} = A/\nu_N. \quad [43]$$

If one takes $\bar{A} \geq 0$ for convenience, then the α electron-spin manifold is represented by the Hamiltonian matrix, $\underline{H}_{N+}$, and β by $\underline{H}_{N-}$. θ and ϕ represent the orientation of the external magnetic field with respect to the nuclear quadrupole axis system.

Figure 1 shows 3D views of the integrated frequency-domain intensity of each nuclear transition of both α and β electron manifolds, defined as the integral over all orientations,

$$I_{\text{s.a.}}^{n(\pm)} = \int_\phi \int_\theta I_{\nu(n\pm)}^{(2)} \frac{\sin\theta}{4\pi}\, d\theta d\phi, \quad [44]$$

as a function of $\bar{A}$ and $\bar{\nu}$. The intensities of the different transitions show some differences in detail, but for all transitions the intensities are large along two approximately perpendicular ridges, $\bar{A} \sim 2$ and $\bar{\nu} \sim 1$. The trend can be examined more readily by investigating the sum of the intensities of the three nuclear transitions within an electron manifold ($I_{\text{s.a.}}^{\pm} = \sum_{n=1}^{3} I_{\text{s.a.}}^{n(\pm)}$), which is the same for the two manifolds. Figure 2 shows this sum in 3D view and as a 2D contour map. As seen in the figure, the strongest intensities are observed along the top of the roughly parabolic ridge connecting the coordinates ($\bar{A}$, $\bar{\nu}$) = (2, 10); (2.5, 1.5); and (10, 0.4).

The vertical portion of the ridge, with $\bar{A} \sim 2$ (for $\bar{\nu} \geq 0.5$), corresponds to the well-known exact/near cancellation case. In this case, the nuclear states in the α manifold become pure nuclear quadrupole states, which are independent of the nuclear quadrupole coupling constant, while those in the β manifold are mostly Zeeman states. This leads to large probabilities for the forbidden EPR transitions and brings strong modulation. However, the intensity rapidly decreases for $\bar{\nu} \leq 0.5$, even at $\bar{A} = 2$, because the nuclear states in both spin manifolds approach pure nuclear quadrupole states in this case (*11*). The new and interesting feature is the strong intensities observed for the horizontal ridge along $\bar{\nu} = \sim$1–0.4 for $\bar{A} \geq 3$. More extended calculation shows that for $\bar{A} \geq 3$ the horizontal ridge is approximated by a hyperbola, $\bar{A} \cdot \bar{\nu}(=A/K) = 4 \sim 5$. Although the figure is limited in the range of $\bar{A} \leq 10$ and $\bar{\nu} \leq 10$ for graphical representation, extended numerical calculations over the ranges reveal the strong intensity ridges of $\bar{A} \sim 2$ and $\bar{A} \cdot \bar{\nu}(=A/K) = 4 \sim 5$ maintain their intensities indefinitely in each direction but with a decreasing width of the ridge.

The shaded [$\bar{A}$, $\bar{\nu}$] region in Fig. 2(B) gives rise to large net ESEEM modulation amplitudes or depth, but the detection of the modulation is strongly dependent not only on its amplitude, but also on the breadth of the transition, namely the spread in frequencies associated with the powder pattern. Figure 3 shows the breadths of the three nuclear transitions in each electron-spin manifold. For $\bar{\nu} \sim 0$, the nuclear states in both manifolds approach the pure nuclear quadrupole states, which are independent of the magnetic field, and thus give narrow bands. In the α manifold these nuclear quadrupole states are also achieved when $\bar{A} \sim 2$ and again the nuclear transitions are narrow. As the couplings move away from the above conditions, $\bar{\nu} \sim 0$ in both manifolds or $\bar{A} \sim 2$ in the α manifold, the nuclear states become m_I states, which are dependent on the magnetic field orientation, and the $\nu_{a\pm}$, $\nu_{b\pm}$ transitions give broad bands. But the sum frequencies ($\nu_{c\pm} = \nu_{a\pm} + \nu_{b\pm}$) are weakly dependent on the external magnetic field and have relatively narrow breadths in both manifolds, as in Figs. 3C and 3F.[2]

In the time domain, the modulation from a nuclear transition

[2] Here, the sum frequency means the nuclear transition whose frequency is the sum of the other two nuclear transition frequencies in an electron-spin manifold ($\nu_{c\pm} = \nu_{a\pm} + \nu_{b\pm}$). In a spin manifold where the nuclear states are mostly nuclear quadrupole states, this sum frequency corresponds to ν_+ and in a spin manifold where the nuclear states are m_I states, this corresponds to double-quantum transition (dq).

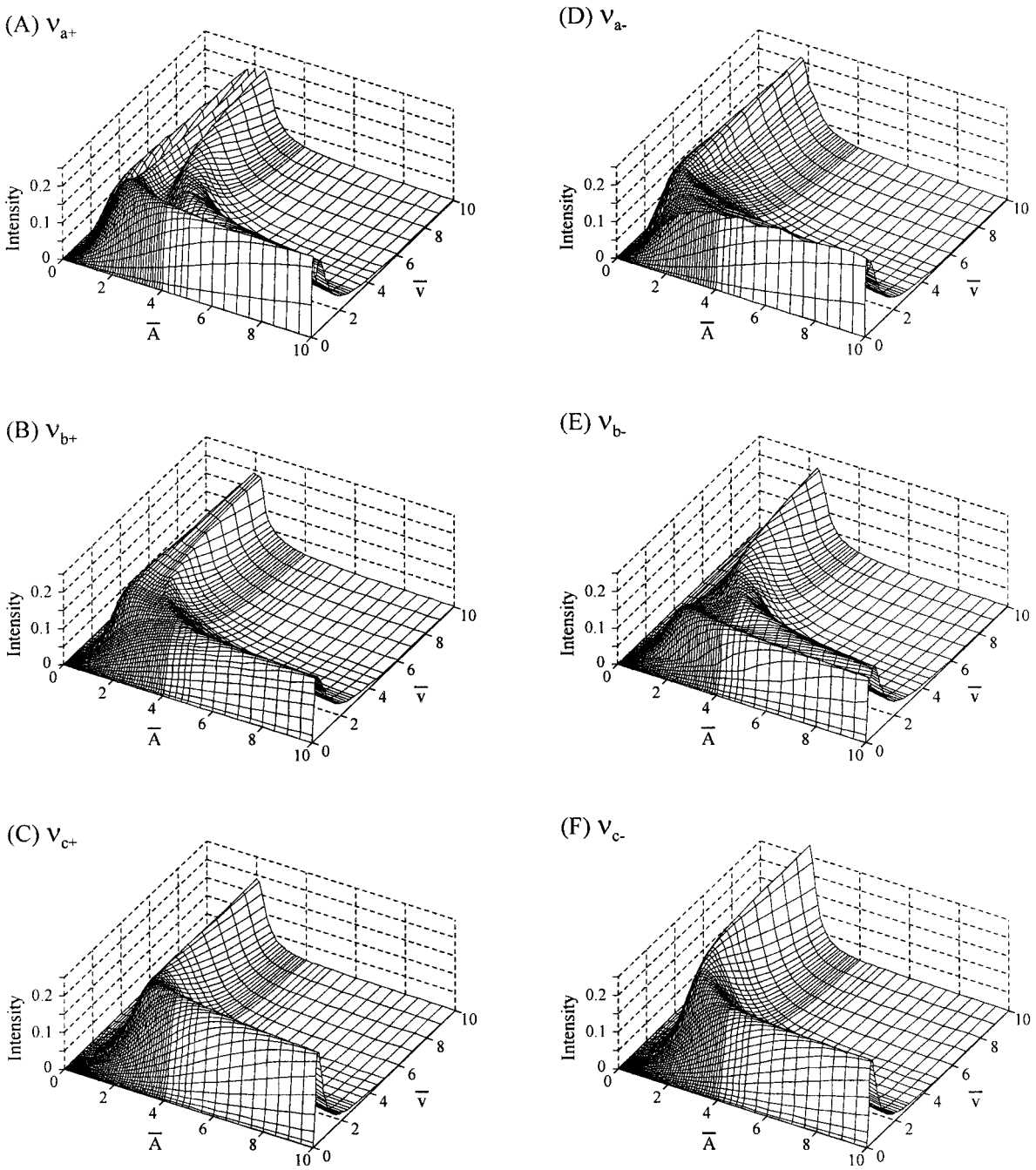

FIG. 1. 3D representation of the spherically averaged frequency-domain intensities ($\int_\phi \int_\theta I^{(2)}_{\nu(n\pm)} \sin\theta/4\pi\, d\theta d\phi$) of nuclear ($I = 1$) transitions as a function of $\bar{\nu}(=\nu_N/K)$ and $\bar{A}$ $(=A/\nu_N)$. + and − represents the α and β electron-spin manifolds. $\nu_a < \nu_b < \nu_c$ and $\nu_c = \nu_a + \nu_b$.

with narrow breadth persists for a long time while the modulation of a broad band damps quickly. Hence, the broad bands are relatively difficult to detect in the time wave unless the spectrometer dead-time is short. Comparing the intensities (modulation amplitudes) and the breadths of the transitions in the frequency-domain for a hyperfine coupling with the exact/near cancellation value of $\bar{A} \sim 2$ (for $\bar{\nu} \geq 0.5$) one expects to easily detect the three transition lines of the α manifold and the sum frequency of the β manifold. However, cases where the horizontal ridge satisfies the hyperbola of $\bar{A} \cdot \bar{\nu} = 4 \sim 5$ (for $\bar{A} \geq 3$) are likely to be detected only through the two sum frequencies.

Similar conclusions are reached when one takes an alternative view of the possibility of detecting an ESEEM transition by calculating the maximum peak height of each transition as in Fig. 4. This figure represents the relative peak height of each nuclear transition as a function of $[\bar{A}, \bar{\nu}]$; the procedure for generating such

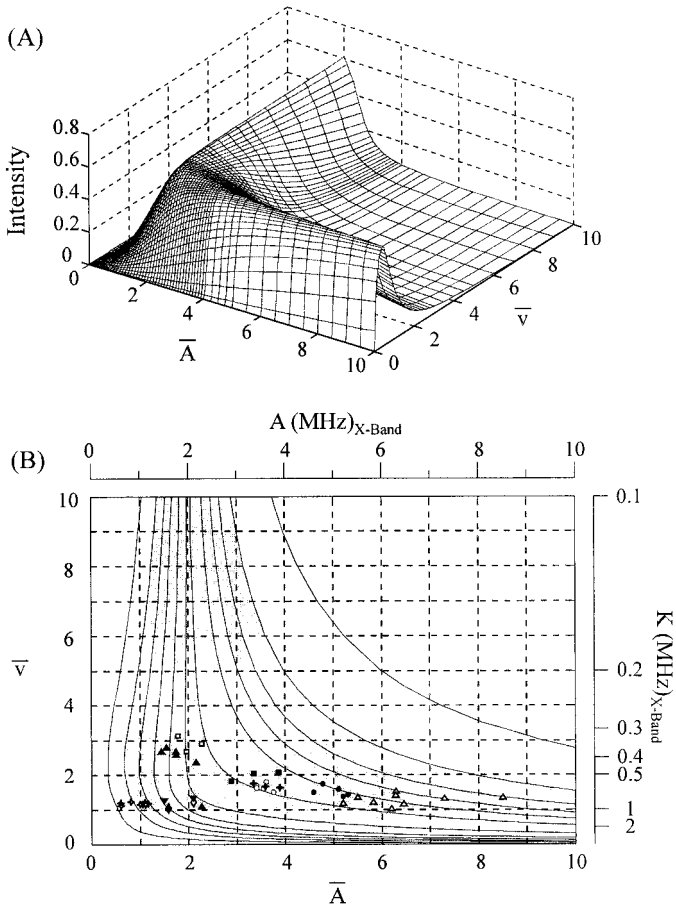

FIG. 2. (A) 3D representation and (B) 2D contour map of sum of the spherically averaged intensities of the three nuclear ($I = 1$) transitions in an electron manifold as a function of $\bar{\nu}$ ($=\nu_N/K$) and $\bar{A}$ ($=A/\nu_N$) ($\Sigma_{n=1}^{3} \int_\phi \int_\theta I^{(2)}_{\nu(n+)} \sin\theta/4\pi\, d\theta d\phi$). Note that $I^{(2)}_{\nu(n+)} = I^{(3)}_{\nu(n+)}$, $I^{(2)}_{\nu(m-)} = I^{(3)}_{\nu(m-)}$ (when $\tau = 0$ for 3-pulse ESEEM), and $\Sigma^{3}_{n=1} I^{(2)}_{\nu(n+)} = \Sigma^{3}_{m=1} I^{(2)}_{\nu(m-)}$ in Eqs. [30]–[33]. The shaded area in (B) represents the $[\bar{A}, \bar{\nu}]$ value regions which can be readily detected by ESEEM before considering the breadth of the nuclear transition. The plots on the 2D contour map represent the $[\bar{A}, \bar{\nu}]$ coordinates of ^{14}N nuclei detected by ESEEM: ○, Rieske center N1 (*44–47*); ●, Rieske center N2 (*44–46*); ◇, peptide nitrogen hydrogenbonded to Fe–S clusters (*48–50*); ◆, methylimidazole coordinated to Co(II)–heme (*51*); □, histidine bound to and CN^-, N_3^- near Mn(III)/Mn(IV) core in X-band (*52*); ■, histidine bound to and CN^-, N_3^- near Mn(III)/Mn(IV) core in P-band (*52*); ◆, CN^- bound to low-spin Fe(III) heme (*53*); ◇, CN^- bound to plastoquinon anion radical (*54*); ▼, trp-trp quinon cofactor radical (*55*); ▲, remote nitrogens of 2-ethylthio-4-hydroxypterin (*56*), imidazole (*57*), and histidine bound to Cu(II) (*58*). Axes at upper and right sides of (B) represent the hyperfine coupling and K values at X-band (3249 G, $\nu_N = 1.0$ MHz).

a 3D representation is depicted in the figure legend. Flanagan and Singel (*11*) thoroughly investigated exact cancellation and derived the range over which the exact/near cancellation condition can be usefully applied. While the plots in Figs. 1 to 4 include their findings, the figures give a more extensive picture of the changes of the intensities of the nuclear transitions as a function of $[\bar{A}, \bar{\nu}]$ and the connectivity of two ridges of strong modulation. Note that $\tilde{K}$ in their paper is the reciprocal of $\bar{\nu}$ ($\tilde{K} = 1/\bar{\nu}$).

Figure 2B includes the $[\bar{A}, \bar{\nu}]$ coordinates for numerous systems that were previously detected by ^{14}N ESEEM. The plot indeed demonstrates many of these observed ^{14}N modulations near the horizontal branch of the hyperbola, $\bar{A} \cdot \bar{\nu} = 4 \sim 5$ and $\bar{A} \geq 3$, as well as the vertical exact/near cancellation ridge. This horizontal regime appears to be analogous to the situation in non-Kramers ^{14}N ESEEM at weak magnetic fields (0 ~ 20 G), where ^{14}N gives strong modulations (*31–33*). The Larmor frequencies at these fields are very small, and as a result such systems exhibit large $\bar{A}$ and tiny $\bar{\nu}$ values. The physical picture and theoretical background for this horizontal ridge with $\bar{A} \cdot \bar{\nu} = 4 \sim 5$ will be discussed in a future publication (*34*).

(iv). Rhombic g- and hyperfine tensors. In the above section, the $I = 1$ modulation amplitude was investigated in the limit of an isotropic **g**-tensor where spherical averaging is applied. However, a spin system with a significant rhombic **g**-tensor requires the collection of a full "2D" field-dependent (orientation-selective) ESEEM or ENDOR pattern to find our the nuclear hyperfine and quadrupole coupling tensors (*1, 3–5*). We first discuss the simplest, nontrivial, case in which **g**-, nuclear hyperfine, and quadrupole tensors are coaxial. Then we generalize to noncoaxial cases. ^{14}N ESEEM patterns of a Kramers-doublet electron-spin system can be classified into two categories: one where $w < 1$ in one manifold (denoted α) and $w > 1$ in the other manifold (denoted β), and the other where $w > 1$ in both manifolds. In this paper, we focus on the first case because the ESEEM pattern of the β manifold covers the second case.

(iv-a). Rhombic g- and hyperfine tensors (coaxial tensors). Figure 5A shows a contour plot of the calculated 2D pattern of frequency vs g for the ^{14}N frequency-domain ESEEM signal in the case of coaxial **g**-, hyperfine, and nuclear quadrupole tensors, with $\mathbf{A} = [2.6\ 2.0\ 1.7]$ MHz, $e^2qQ = 2.1$ MHz, and $\eta = 0.6$. The α spin manifold where $w < 1$ for all orientations shows three distinct peaks (ν_2, ν_3, and ν_1 in Muha's notation, or ν_0, ν_-, and ν_+ in conventional notation) across the EPR envelope, while the β manifold gives only the double-quantum peak as a dominant feature because $w > 1$. The single-quantum bands of the β manifold are omitted from the figure because the transitions are broad, so that their intensities are too weak to be analyzed in a real experimental situation except for ESEEM at the "single-crystal-like" edges (g_x and g_z). Overall the ESEEM pattern is similar to the well-known ^{14}N ESEEM pattern of near cancellation where sharp ν_2, ν_3, ν_1 features are seen for the $w < 1$ (α) manifold and only dq is seen for the other manifold, but the rhombic hyperfine tensor causes additional features. In the full 2D display of g-value and frequency (Fig. 5A), the contour map of each band in the α manifold (ν_1, ν_2, and ν_3) spreads out at g-values away from the single-crystal-like edges (g_x and g_z) and makes a "triangular" shape with the maximum breadth at $g = g_y$.

The three vertices are at (ν_{nx}, g_x), (ν_{ny}, g_y), and (ν_{nz}, g_z) [$n = 1, 2, 3$] for each ν_n pattern corresponding to the orientation where the field lies along the principal axis orientations of the tensors. The frequencies of the vertices are obtained in analytical form (Table 1) by adapting Muha's

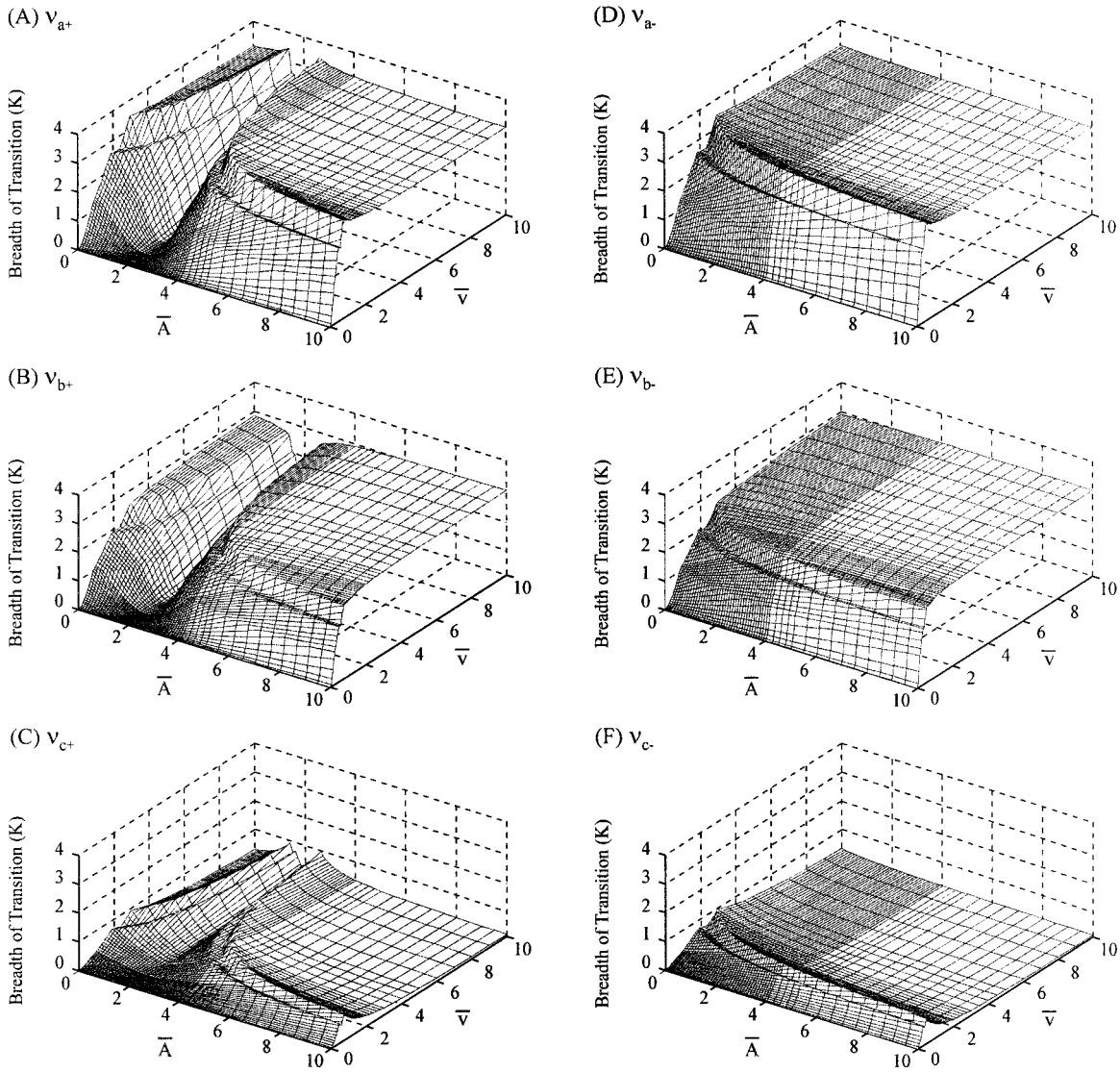

FIG. 3. The breadths of the nuclear ($I = 1$) transitions arising from powder sample. The breadth was obtained by ($\nu_{max} - \nu_{min}$) of each nuclear transition from powder pattern.

solutions in which the reference frame is the nuclear quadrupole axis (*8, 9, 35*). When one uses these equations in Table 1, it is important to label the frequencies consistently. As seen in Table 1, $\nu_1 > \nu_3 > \nu_2$ (Eq. [29]) always hold at g_x independent of the relative size of the hyperfine, nuclear quadrupole couplings, and the nuclear Larmor frequency, because $0 < \eta < 1$ by definition. But at the other field positions, the relative frequencies depend on the magnitude of the couplings. Hence, even for correct assignment of nuclear transition bands, field-dependent ESEEM is often necessary.[3] The dq band also exhibits a triangle-like shape with each edge of the triangle corresponding to a peak in the spectra, and the frequencies can be obtained by Muha's solution (Table 1).

In orientation-selective ESEEM, just as in a spherically averaged experiment, the ESEEM frequencies of the α manifold are sensitive to the nuclear quadrupole couplings but not to the hyperfine couplings because the hyperfine couplings and nuclear Zeeman interaction are largely canceled out, while the dq frequency in the β electron spin state is sensitive to the nuclear hyperfine interactions. Through use of the equations in Table 1, the nuclear quadrupole parameters for coaxial **g**-, the

[3] Muha's frequency assignment of ν_1, ν_2, ν_3 bands always holds across the EPR envelope when $w < 1$ because the nuclear spin states are mostly the nuclear quadrupole states. But, for the dq band where $w > 1$, the nuclear spin states are mostly m_I states, $|-1\rangle$, $|0\rangle$, $|+1\rangle$, and the dq band corresponds to the outer transition, $|-1\rangle \leftrightarrow |+1\rangle$. If we use Muha's formulas, the assignment of the dq transition depends on the relative sizes of w and η. The dq ($w > 1$) always corresponds to ν_1 except that it is ν_3 for $w(=|(-\nu_N - A_y/2)/K|) > (6\eta + 2\eta^2)^{1/2}$ along y-axis, and ν_2 for $w(=|(-\nu_N - A_z/2)/K|) > (9 - \eta^2)^{1/2}$ along z-axis.

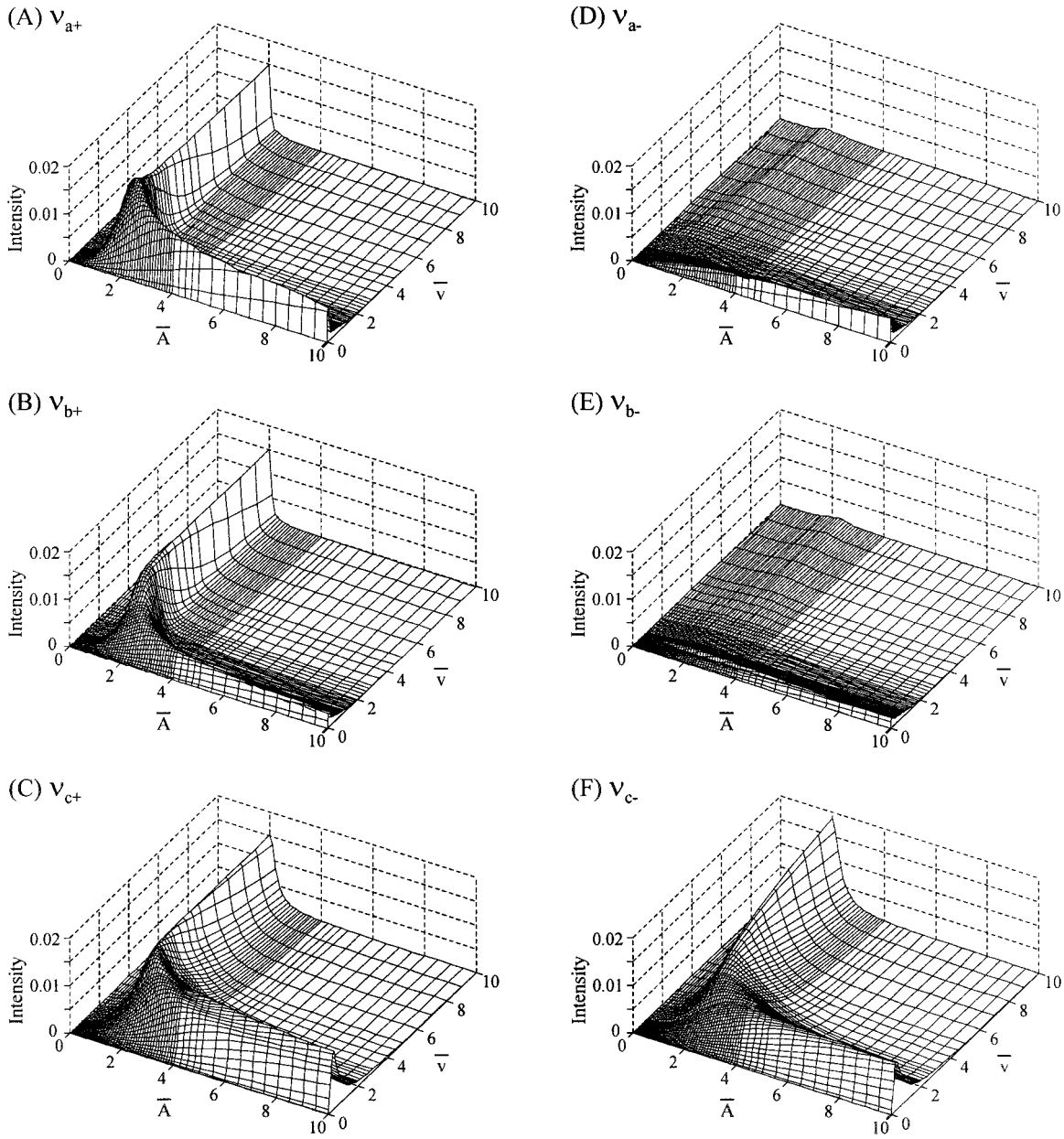

FIG. 4. The 3D representation of the maximum peak height of each nuclear transition. The figure is constructed as follows. First, a histogram of the intensity ($I^{(2)}_{n\pm}$ sin $\theta/4\pi$) was built on a frequency-domain (unit of K) with given values of [$\bar{A}$, $\bar{\nu}$]. Secondly, the histogram was convoluted with a Gaussian function with a finite half width (here 0.07 K). Then the maximum peak height was selected. This procedure was repeated as a function of [$\bar{A}$, $\bar{\nu}$].

nuclear hyperfine, and the quadrupole tensors can be calculated directly from the frequencies measured at g_x and g_z, with

$$K = (\nu_{1\pm} + \nu_{3\pm})/6, \text{ at } g_z \quad [45]$$

$$\eta = 1 - (\nu_{3\pm} - \nu_{2\pm})/3K, \text{ at } g_x. \quad [46]$$

The nuclear hyperfine tensor components (A_x, A_y, A_z) can then be derived to high accuracy by using K, η, and Muha's formulas for the dq band (Table 1).

The importance of using a proper analysis and not relying on assumptions of exact/near cancellation is seen as follows. According to the exact/near cancellation analysis where the low, middle, and high frequency peaks are assigned to ν_o, ν_-, and ν_+, respectively, the nuclear quadrupole coupling parameters are given by (*10*, *36*)

$$K = (\nu_- + \nu_+)/6 \quad [47]$$

$$\eta = \nu_o/2K. \quad [48]$$

If one attempts to apply this analysis to the calculated spectra

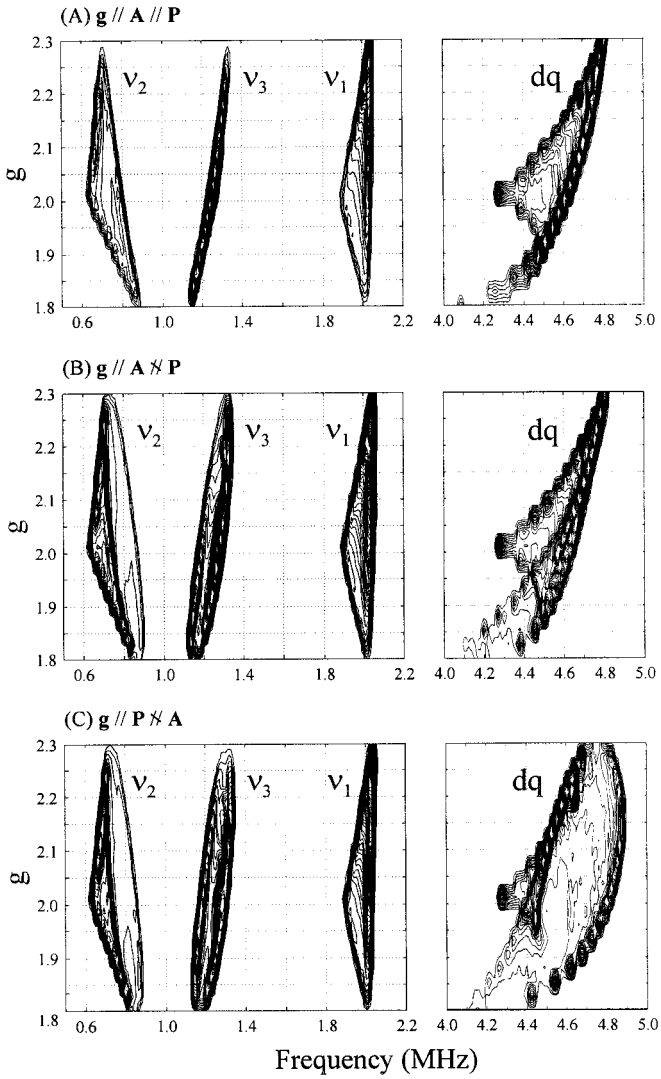

FIG. 5. 2D contour map of ESEEM simulation as a function of g-value and nuclear transition frequency. Simulation parameters: microwave frequency = 9.5 GHz, **g** = [2.3 2.01 1.8], **A** = [2.6 2.0 1.7] MHz, e^2qQ = 2.1 MHz, and η = 0.6. ESEEM linewidth (Gaussian) is 0.05 MHz. Relative orientations of **g**-, hyperfine (**A**), and nuclear quadrupole (**P**) tensors are (A) **g**‖**A**‖**P**, (B) **g**‖**A**/‖**P**, **P**-tensor rotates 15° from **g**-tensor about g_y, $\angle(g_z \sim P_{ZZ})$ = 15°, and (C) **g**‖**P**/‖**A**, **A**-tensor rotates 15° from **g**-tensor about g_y, $\angle(g_z \sim A_z)$ = 15°. EPR linewidth is assumed to be zero.

of Figure 5A, then the spectrum at g_x gives e^2qQ = 2.26 MHz, η = 0.63, whereas that at g_z gives e^2qQ = 2.1 MHz, η = 0.843. Both calculated parameters differ from the input values of e^2qQ = 2.1 MHz, η = 0.6.[4]

When $w > 1$ in both α and β spin manifolds, the nuclear spin states in both manifolds are mostly m_I states, and ESEEM from both manifolds show the same characteristics as for the β manifold of the previous case. Therefore, one expects spectra to be dominated by two double-quantum transition lines, one from each m_s spin manifold, while the single-quantum lines from both manifolds will be broad and weak. If the single-quantum peaks from ESEEM spectra obtained at single-crystal-like g-value positions (g_x and g_z) are detected, the analysis will follow the previous case. Otherwise, the nuclear quadrupole coupling parameters may not be well determined.

(iv-b). Rhombic g- and hyperfine tensors (noncoaxial tensors). Figure 5B shows the effect on the ^{14}N ESEEM pattern of rotating the nuclear quadrupole axes, while preserving the coaxial orientation of the nuclear hyperfine tensor with **g**-tensor, as in Fig. 5A. In the numerical calculation for Fig. 5B, the nuclear quadrupole principal axis (P_{ZZ}) lies in the $g_x - g_z$ plane (rotating about the g_y or P_{YY} axis); the angle between the g_z axis and P_{ZZ} axis is set to be 15°. In Fig. 5A, where all tensors are coaxial, the lines of the triangles are almost straight and represent single-frequency turning points ($(d\nu/ds)_g = 0$, where s represents the path satisfying $g(\theta, \phi) = g$). As discussed in great detail in earlier analyses of orientation-selective ENDOR (*1, 3–5*), when the nuclear quadrupole axes are rotated in the $g_x - g_z$ plane (about g_y) as in Fig. 5B, the mixing of P_{XX} and P_{ZZ} causes the peak represented by the line in Fig. 5A that connects $[\nu_{nx}, g_x]$ and $[\nu_{nz}, g_z]$ to split into two, and the vertex frequencies no longer are given by Table 1. Comparing Figs. 5A and 5B clearly shows this behavior for ν_2 and ν_3; for this choice of a modest rotation, the splitting is not well observed in the ν_1 band. If the nuclear quadrupole axis (P_{ZZ}) is located between the g_y and g_z axes, the lines connecting $[\nu_{2y}, g_y]$ and $[\nu_{2z}, g_z]$ for ν_2 band and $[\nu_{3y}, g_y]$ and $[\nu_{3z}, g_z]$ for ν_3 band are split instead. Figure 5B shows that the pattern for the dq band also changes in very similar ways to the fundamental bands of the α spin manifold. Because the quadrupole tensor is rotated in the $g_x - g_z$ plane (about g_y), the outermost turning-point curve connecting g_x and g_z is split into two curves.

Figure 5C presents the ESEEM pattern when the **g**- and the nuclear quadrupole tensor remain coaxial, but the nuclear hyperfine tensor is rotated about the g_y or A_y axis so that the A_z axis is on $g_x - g_z$ plane. Compared with Fig. 5B where the nuclear quadrupole axes are rotated, the bands in the α manifold (ν_1, ν_2, ν_3) look the same in both cases because the pattern is determined by the relative orientation of the nuclear hyperfine and quadrupole tensors, but the dq bands in the β manifold look different because this pattern is determined by the relative orientation of the **g**- and the hyperfine tensors. A closer look at the dq bands in Figs. 5B and 5C shows that the overall behavior of the ESEEM pattern is similar: the curves connecting $[\nu_{\mathrm{dq}\,x}, g_x]$ and $[\nu_{\mathrm{dq}\,z}, g_z]$ are split into two in both figures.

When the three tensors, **g**, **A**, and **P**, are not all coaxial, the ESEEM pattern becomes still more complicated, with other lines in Fig. 5A splitting upon rotations involving additional Euler angles (around other **g**-tensor axes). The principles governing these effects are the same as those that determine orientation-selective ENDOR pattern (*1, 3–5*). The procedures by which the 2D patterns are fit involve generating the best possible description using coaxial tensors, then introducing the minimal number of

[4] The discrepancy of double-quantum frequencies in between orientation-selective and spherically averaged spectra was noticed by Fukui *et al.* (*35*).

TABLE 1
ESEEM Frequencies of the System with $S = \frac{1}{2}$ and $I = 1$ for g//A//P

g-value	Frequencies[a] $n = \pm 1$	$n = \pm 2$	$n = \pm 3$
g_x[b]	$[4(-\nu_N \pm A_x/2)^2 + (3 + \eta)^2K^2]^{1/2}$	$\{-3(1 - \eta)K + [4(-\nu_N \pm A_x/2)^2 + (3 + \eta)^2K^2]^{1/2}\}/2$	$\{3(1 - \eta)K + [4(-\nu_N \pm A_x/2)^2 + (3 + \eta)^2K^2]^{1/2}\}/2$
g_y[c]	$\{3(1 + \eta)K + [4(-\nu_N \pm A_y/2)^2 + (3 - \eta)^2K^2]^{1/2}\}/2$	$\{3(1 + \eta)K - [4(-\nu_N \pm A_y/2)^2 + (3 - \eta)^2K^2]^{1/2}\}/2$	$[4(-\nu_N \pm A_y/2)^2 + (3 - \eta)^2K^2]^{1/2}$
g_z[b]	$3K + [(-\nu_N \pm A_z/2)^2 + \eta^2K^2]^{1/2}$	$2[(-\nu_N \pm A_z/2)^2 + \eta^2K^2]^{1/2}$	$3K - [(-\nu_N \pm A_z/2)^2 + \eta^2K^2]^{1/2}$

[a] Either + or − indicates $m_s = -\frac{1}{2}$ or $+\frac{1}{2}$ electron spin manifold, respectively.
[b] Single-crystal-like spectrum.
[c] The frequencies represent only the orientation of $\mathbf{H}_o$//y-axis out of all the magnetic field orientations satisfying $h\nu_{MW} = g_y\beta_e H_o$.

rotations needed to satisfactorily describe the results. In the Appendix we present sample ESEEM calculations in which no two interaction tensors are coaxial (Fig. A1).

(v). ^{14}N ESEEM of nitrogenase MoFe protein. The resting state FeMo-cofactor of the nitrogenase MoFe protein shows a $S = \frac{3}{2}$ EPR signal ($g'_{x,y,z} = 4.33, 3.77, 2.01$). Previous ESEEM studies of nitrogenase from *Clostridium pasteurianum* and *Azotobacter vinelandii* (*Av*1) revealed strong ^{14}N modulations (*23*, *37*, *38*). In those studies, the ESEEM spectra were collected and analyzed at only a few g-value positions. The spectra showed four ESEEM lines, as is found under near cancellation conditions, and their approximate analysis was not based on the full orientation-selective ESEEM approach. To achieve a complete analysis, we collected three-pulse, stimulated ESEEM spectra at numerous field positions across the EPR envelope of *Av*1 as shown in Fig. 6A ($\tau \sim 200$ ns, the time interval between the first and the second pulses). As mentioned in Section (i-b), because the transformation to fictitious spin $S' = \frac{1}{2}$ introduces anisotropic behavior into the hyperfine interaction even if the intrinsic coupling is isotropic, the complete analysis of the nitrogenase ^{14}N ESEEM must be performed by following the method developed in Section (iv).

While the individual ESEEM spectra in Fig. 6A appear typical of near cancellation, the 2D pattern exhibited by spectra collected across the EPR spectrum indicates a more complicated situation. According to the discussion of rhombic tensors in the above sections, from low to high frequency we assign the ν_2, ν_3, and ν_1 bands to one electron-spin manifold and the dq band to the other manifold. As seen in the figure, at g_x the ^{14}N modulation is dominated by the ν_1 and dq bands. The 2D patterns for ν_2, ν_1, and most especially the dq band show a triangle-like shape characteristic of a rhombic ^{14}N hyperfine interaction, with maximum breadth at g_y. Note further that the ν_2 and ν_3 bands cross each other at $g \sim 2.2$. Finally, the modulation almost disappears at g_z. In addition to the strong peaks (shaded) in the wild-type (Fig. 6A) and mutant proteins (Fig. A2), there are also weak features. Those could be single-quantum peaks, arising from orientation selection, from the electron manifold that gives the dq band. However, because more than one ^{14}N nucleus gives rise to the modulation in these proteins, and the shaded features are enough to analyze the spectra, we do not consider other features.

If we begin by assuming that all the interactions are coaxial (**g′**-, hyperfine, and nuclear quadrupole tensors), the first step is analysis of the frequencies at the three vertices of the triangular patterns in the 2D (frequency vs g') ESEEM; those frequencies, as measured from Fig. 6A, are collected in Table 2. The nuclear quadrupole parameters then are obtained by adapting Eqs. [45] and [46] as

$$K = (\nu_1 + \nu_3)/6 = 0.54 \text{ MHz at } g'_z$$
$$\eta = 1 - (\nu_3 - \nu_2)/3K = 0.59 \text{ at } g'_x.$$

The dq band is more sensitive to the hyperfine tensor values, and from Muha's frequency formulas (Table 1) (*9*, *35*),

$$\text{dq} = [4(-\nu_N + A'_x/2)^2 + (3 + \eta)^2K^2]^{1/2} = 3.65 \text{ MHz at } g'_x,$$

$$\text{dq} = [4(-\nu_N + A'_y/2)^2 + (3 - \eta)^2K^2]^{1/2} = 3.31 \text{ MHz at } g'_y,$$

$$\text{dq} = 2[(-\nu_N + A'_z/2)^2 + \eta^2K^2]^{1/2} = 3.3 \text{ MHz at } g'_z,$$

which gives $[A'_x, A'_y, A'_z] = [2.11, 1.93, 1.17]$ MHz. The hyperfine values thus obtained are in the fictitious spin representation. Since the intrinsic g-values ($S = \frac{3}{2}$) for *Av*1 deviate negligibly from $g = 2.0$, the intrinsic hyperfine values, as calculated from Eq. [12], become

$$A'_j = A_j g'_j/g_j = A_j g'_j/2, \quad [49]$$

which gives $[A_x, A_y, A_z] = [0.98, 1.02, 1.14]$ MHz.

Using the equations presented above, the ^{14}N ESEEM spec-

tra were simulated with the values of the experimentally derived nuclear quadrupole tensor and the hyperfine tensor. The contour map of the simulation is displayed on a 2D plot in Fig. 6B. In the simulation, the pseudonuclear Zeeman effect was included, but the ^{14}N nuclear hyperfine coupling constant is too small to give rise to any observable effect ($3g_e\beta_e A/2g_N\beta_N\Delta = 0.075$, see Eqs. [14] and [16]). The simulation with all tensors coaxial shows a good fit to the experimental data, and this was confirmed by extensive calculations with noncoaxial tensors, which were performed to test the assumption of coaxial tensors. The simulations yielded the intrinsic hyperfine interaction tensor, $[A_x, A_y, A_z] = [0.98\ (0.03), 1.02\ (0.03), 1.14\ (0.09)]$ MHz, and quadrupole parameters, $e^2qQ = 2.17\ (0.13)$ MHz, and $\eta = 0.59\ (0.07)$, with all tensors indeed coaxial with the $\mathbf{g}'$-frame (fine structure) (Table 3). The uncertainty of the rotation angles (noncoaxiality) is also included in Table 3. The previous approximate analysis yielded quadrupole values of, $e^2qQ = 2.2$ MHz and $\eta = 0.5$ (*23*), in good agreement with those reported here.

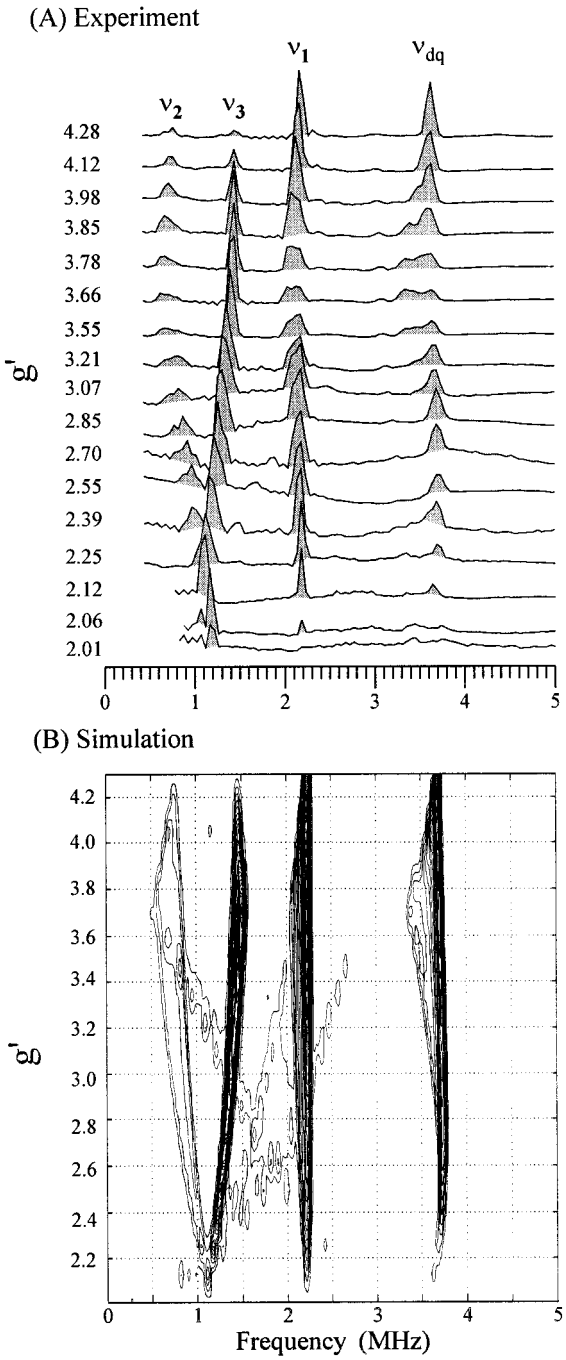

FIG. 6. (A) Field-dependent three-pulse ESEEM FT spectra obtained across the EPR spectrum of wild-type MoFe protein and (B) corresponding simulation. Experimental conditions: microwave frequency, 9.547 GHz; τ = 124 ~ 152 ns. Simulation parameters: A = [0.98 1.02 1.14] MHz, e^2qQ = 2.17 MHz, and $\eta = 0.59$ with $\tau = 150$ ns and a Gaussian linewidth of 0.05 MHz. All the tensors are coaxial. Data and simulation are reproduced from Ref. (*22*).

TABLE 2
Observed X-Band ^{14}N ESEEM Frequencies of MoFe Protein

	Frequency (MHz)					
g′-value	ν_1	ν_2	ν_3	dq	H (G)	ν_N (MHz)
4.33 (g'_x)[a]	2.24	0.78	1.46	3.65	1587	0.488
3.77 (g'_y)[b]	2.04	0.58	1.46	3.31	1796	0.553
2.01 (g'_z)[a]	2.19	1.12	1.07	3.3	3412	1.050

[a] Single-crystal-like spectrum.
[b] The frequencies are the values at the vertices of each triangular ESEEM band in 2D domain. (See Theory and Application.)

For a system with noncoaxial tensor, the analytical extraction of the tensor values as above is not possible. But, as in ENDOR spectroscopy, we can still derive the values by simulating a 2D, $[g, \nu]$, pattern using the procedure presented in the above Section (iv). In fact, the analysis of ^{14}N ESEEM from some mutants of the MoFe protein yielded noncoaxial tensors in some cases. Table 3 includes the hyperfine and quadrupole parameters for several mutants of the wild-type MoFe protein; the experimental data and simulations for these mutants are displayed in Fig. A2 of the Appendix.

EXPERIMENTAL

The nitrogenase MoFe protein was prepared as previously described (*39–41*). Three-pulse or stimulated electron spin echoes were obtained on a locally constructed pulsed EPR spectrometer described elsewhere, with pulse width of 16 ns and pulse power of ~1 W (*42*). Three-pulse ESEEM time domain data were collected by changing the time interval (T) between the second and the third pulses at $2K$. The frequency-domain ESEEM spectra were obtained by Fourier transformation (FT) of the time domain data. The FT was accompanied with modified Mims' "dead time" reconstruction routine (*43*). Computer simulation programs were written in MATLAB soft-

TABLE 3

^{14}N Hyperfine and Nuclear Quadrupole Coupling Tensors of Wild-Type and Mutant Nitrogenase MoFe Proteins[a]

	Hyperfine coupling[c]		Nuclear quadrupole coupling[c]		
Mutants[b]	Tensor (MHz)[d]	Orientation (°)[e]	e^2qQ	η	Orientation (°)[e]
Wild-type α-195^{Gln} α-96^{Lys}	0.98 (3), 1.02 (3), 1.14 (9)	0, 0, 0	2.17 (13)	0.59 (7)	0, 0, 0
α-96^{Gln} α-359^{Lys} α-195^{Asn}	0.4 (1), 0.5 (3), 0.4 (3)	[f]	3.5 (1)	0.35 (5)	0, 60, 20
α-381^{Leu} α-381^{Ile} α-381^{Val}	0.4 (1), 0.6 (3), 0.4 (3)	[f]	3.4 (1)	0.40 (5)	0, 60, 20

[a] Reproduced from Ref. (*22*).

[b] Each mutant MoFe protein is designated by the name of the subunit (α in this case), the number of the amino acid position substituted, followed by the three-letter code for the substituting amino acid in superscript form.

[c] The values in parentheses are the uncertainty limit in the last digits.

[d] The tensor values are the intrinsic hyperfine coupling values (A_{int}) in the real spin, $S = \frac{3}{2}$, representation (See Eq. [49]).

[e] Euler angles (α, β, γ) with respect to the **g**-tensor frame. Limit of the uncertainty is $\pm 10°$ (*26*, *27*).

[f] Because anisotropic portion of the hyperfine tensor is small, **g** and the hyperfine tensors are set to be coaxial.

ware of The MathWorks, Inc. All calculations were performed on PC compatible computers.

CONCLUSION

We have presented general equations for analyzing orientation-selective ^{14}N ($I = 1$) ESEEM from a Kramers doublet with **g**-resolved EPR spectra. We first used them to reexamine the modulation amplitudes as a function of the nuclear hyperfine (A) and quadrupole (K) coupling constants relative to the nuclear Zeeman interaction (ν_N) in the case of isotropic g- and hyperfine interaction. In addition to the well-known near/exact cancellation case that gives rise to strong modulation for isotropic hyperfine coupling when $A/2 \sim \nu_N$ ($\bar{A} \sim 2$), we find another condition, $\bar{A} \cdot \bar{\nu}$ ($= A/K$) $= 4 \sim 5$ (for $\bar{A} \geq 3$), which gives rise to strong modulation. Second, we described a general approach to the analysis of orientation-selective ESEEM spectra to permit analysis for rhombic **g**- and nuclear hyperfine tensors. Calculations of 2D, [g, ν], ^{14}N ESEEM patterns were presented in the cases of coaxial and noncoaxial tensors (**g**-, nuclear hyperfine, and quadrupole tensors). Analytical solutions were derived for the ^{14}N-hyperfine and the quadrupole tensors when the tensors are coaxial with the **g**-tensor reference frame. Finally, based on the procedure developed, the ^{14}N ESEEM of nitrogenase MoFe protein and several of its mutants was analyzed to obtain the hyperfine and nuclear quadrupole tensor for ^{14}N nuclei that interact with the FeMo-cofactor.

ACKNOWLEDGMENTS

This work was supported by the NSF(MCB-9507061) and USDA (97-35305-4879). We thank Profs. D. R. Dean, W. E. Newton, and W. H. Orme-Johnson for the nitrogenase samples.

APPENDIX

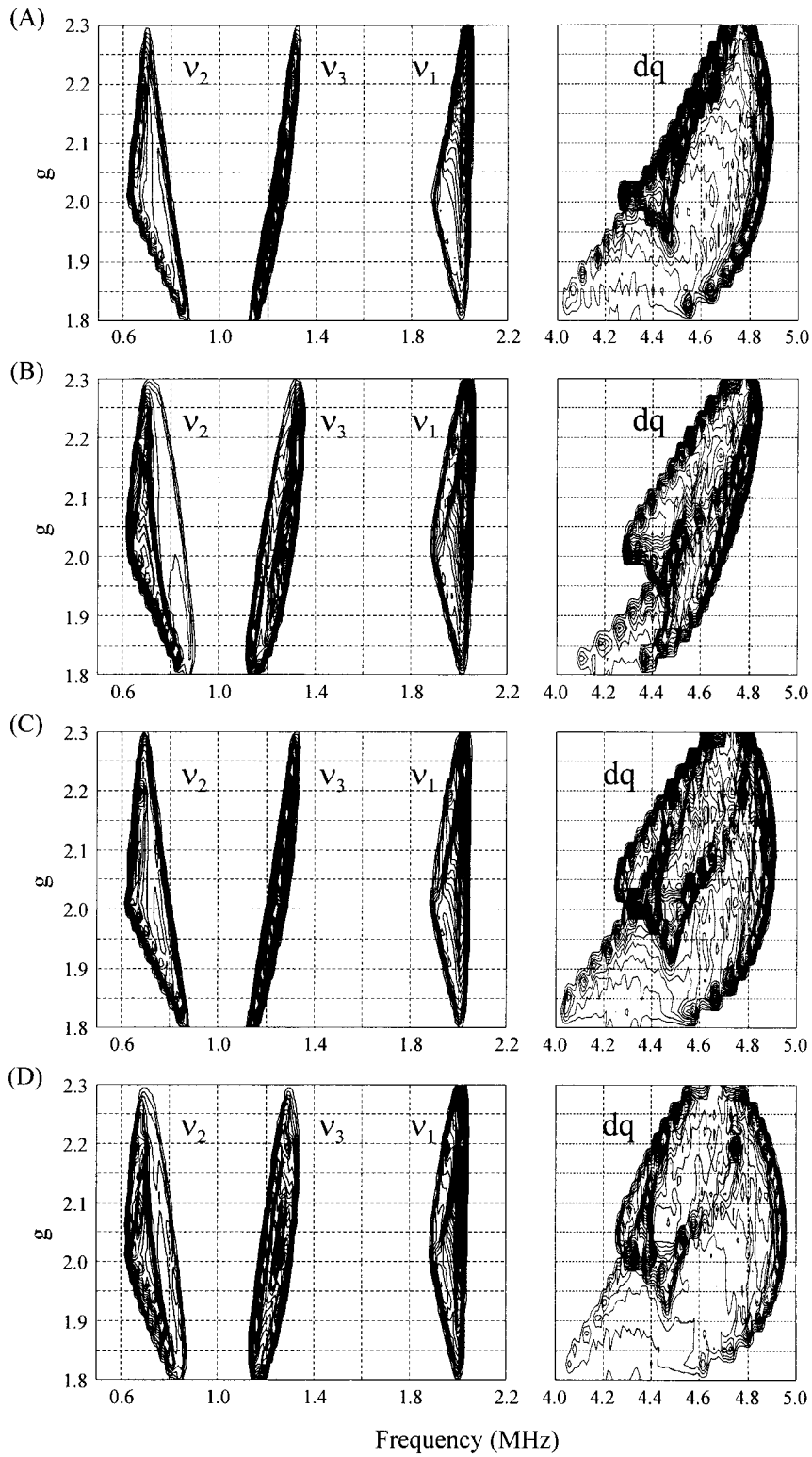

FIG. A1. 2D contour map of ESEEM simulation as a function of **g**-value and nuclear transition frequency. Simulation Parameters: microwave frequency = 9.5 GHz, **g** = [2.3 2.01 1.8], **A** = [2.6 2.0 1.7] MHz, e^2qQ = 2.1 MHz, and η = 0.6. ESEEM linewidth (Gaussian) is 0.05 MHz. Relative orientations of **g**-, hyperfine (**A**), and nuclear quadrupole (**P**) tensors are (A) **g** ∦ **A** ∥ **P**, Euler angles (α, β, γ) (26, 27) of **A**- and **P**-tensors with respect to **g**-tensor, [0 15° 0], (B) **g** ∦ **A** ∦ **P**, Euler angles of **A**-tensor, [15° 0 0], Euler angles of **P**-tensor with respect to **g**-tensor, [0 15° 0], (C) **g** ∦ **A** ∥ **P**, Euler angles of **A**- and **P**-tensors with respect to **g**-tensor, [15° 15° 0], and (D) **g** ∦ **A** ∦ **P**, Euler angles of **A**-tensor, [20° 20° 0], Euler angles of **P**-tensor with respect to **g**-tensor, [10 10° 0]. EPR linewidth is assumed as zero.

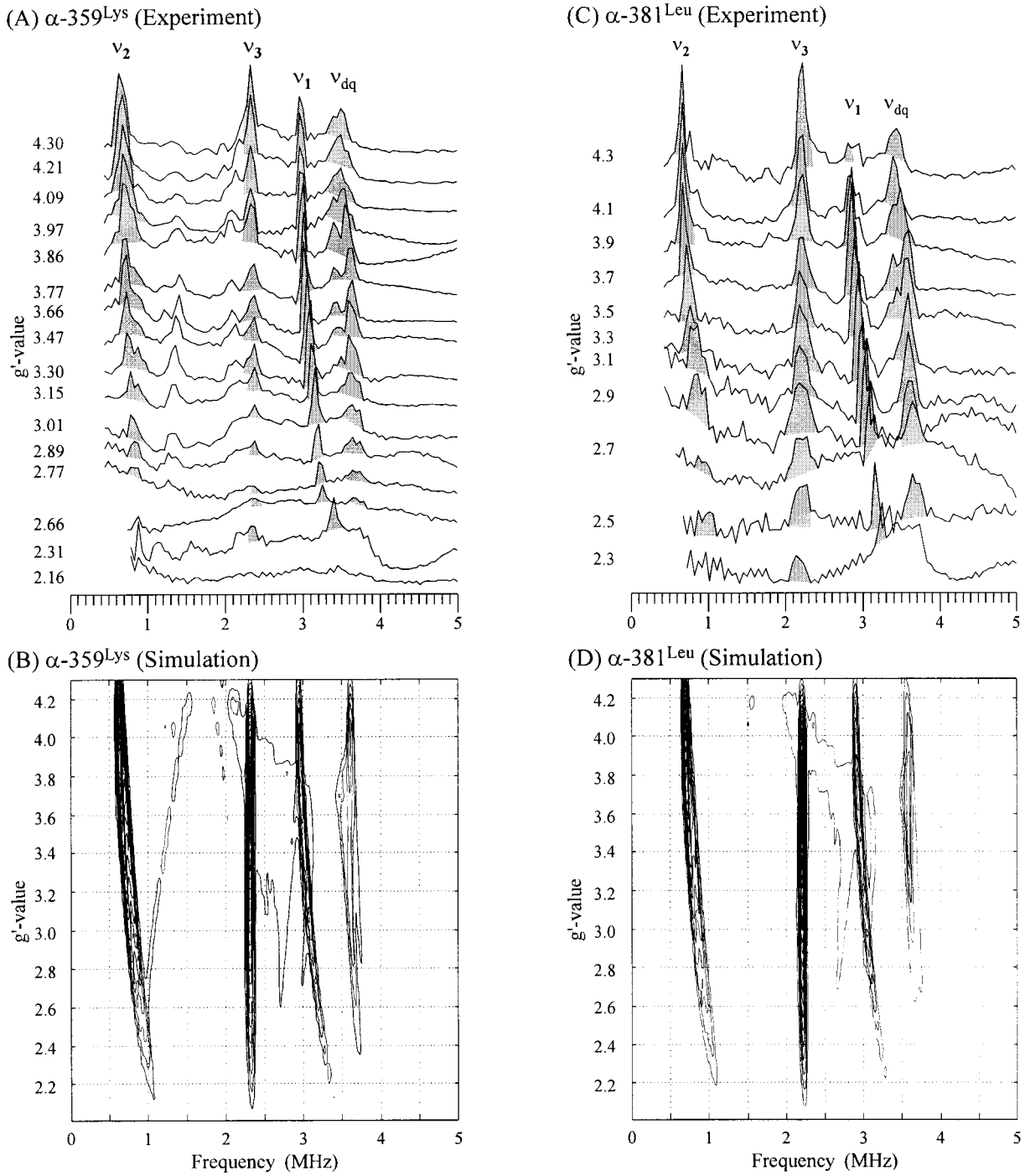

FIG. A2. Field-dependent three-pulse ESEEM FT spectra obtained across the EPR spectra of the (A) α-359^{Lys} and (C) α-381^{Leu} MoFe proteins and (B, D) corresponding simulations. Experimental conditions: microwave frequency, (A) 9.640 and (C) 9.611 GHz; $\tau = 124 \sim 152$ ns. Simulation parameters: $\tau = 150$ ns, for (B) $\mathbf{A} = [0.4\ 0.5\ 0.4]$ MHz, $e^2qQ = 3.5$ MHz, and $\eta = 0.35$, and for (D) $\mathbf{A} = [0.4\ 0.6\ 0.4]$ MHz, $e^2qQ = 3.4$ MHz, and $\eta = 0.40$. In the simulations, **g**- and the hyperfine tensors are coaxial and Euler angles (α, β, γ) of nuclear quadrupole tensor with respect to **g**-tensor are [0° 60° 20°] in both mutants. A Gaussian linewidth of 0.05 MHz are used. Data and simulation are reproduced from ref. 22.

REFERENCES

1. B. M. Hoffman, V. J. DeRose, P. E. Doan, R. J. Gurbiel, A. L. P. Houseman, and J. Telser, Metalloenzyme active-site structure and function through multifrequency CW and pulsed ENDOR, *in* "EMR of Paramagnetic Molecules" (L. J. Berliner and J. Reuben, Eds.), pp. 151–218, Plenum Press, New York (1993).
2. S. A. Dikanov and Y. D. Tsvetkov, "Electron Spin Echo Envelope Modulation (ESEEM) Spectroscopy," CRC Press, Boca Raton, FL (1992).
3. B. M. Hoffman, R. A. Venters, and J. Martinsen, *J. Magn. Reson.* **62,** 537–542 (1985).
4. B. M. Hoffman, J. Martinsen, and R. A. Venters, *J. Magn. Reson.* **59,** 110–123 (1984).
5. V. J. DeRose and B. M. Hoffman, *Methods Enzymol.* **246,** 554–589 (1995).
6. W. B. Mims, *Phys. Rev. B* **5,** 2409–2419 (1972).
7. W. B. Mims, *Phys. Rev. B* **6,** 3543–3545 (1972).
8. G. M. Muha, *J. Chem. Phys.* **73,** 4139–4140 (1980).
9. G. M. Muha, *J. Magn. Reson.* **49,** 431–443 (1982).
10. A. V. Astashkin, S. A. Dikanov, and Y. D. Tsvetkov, *Zh. Struc. Khim.* **25,** 53–64 (1984).
11. H. L. Flanagan and D. J. Singel, *J. Chem. Phys.* **87,** 5606–5616 (1987).
12. E. J. Reijerse and C. P. Keijzers, *J. Magn. Reson.* **71,** 83–96 (1987).
13. A. M. Tyryshkin, S. A. Dikanov, and E. J. Reijerse, *J. Magn. Reson. A* **116,** 10–21 (1995).
14. S. A. Dikanov, V. F. Yudanov, and Y. D. Tsvetkov, *J. Magn. Reson.* **34,** 631 (1979).
15. L. Kevan, *J. Phys. Chem.* **88,** 327 (1984).
16. H.-I. Lee and J. McCracken, *J. Phys. Chem.* **98,** 12861–12870 (1994).
17. J. McCracken and S. Friedenberg, *J. Phys. Chem.* **98,** 467–473 (1994).
18. H. L. Flanagan, G. J. Gerfen, A. Lai, and D. L. Singel, *J. Chem. Phys.* **88,** 2161–2168 (1988).
19. P. J. van Dam, E. J. Reijerse, M. J. van der Meer, R. Guajardo, P. K. Mascharak, and E. de Boer, *Appl. Magn. Reson.* **10,** 71–86 (1996).
20. E. J. Reijerse, A. M. Tyryshkin, and S. A. Dikanov, *J. Magn. Reson.* **131,** 295–309 (1998).
21. S. A. Dikanov, A. M. Tyryshkin, J. Huttermann, R. Bogumil, and H. Witzel, *J. Am. Chem. Soc.* **117,** 4976–4986 (1995).
22. H.-I. Lee, S. T. Kristin, D. R. Dean, W. E. Newton, and B. M. Hoffman, *Biochemistry* **37,** 13370–13378 (1998).
23. V. J. Derose, C. H. Kim, W. E. Newton, D. R. Dean, and B. M. Hoffman, *Biochemistry* **34,** 2809–2814 (1995).
24. A. Abragam and B. Bleaney, "Electron Paramagnetic Resonance of Transition Ions," 2nd ed., Clarendon Press, Oxford (1970).
25. M. K. Bowman and R. J. Massoth, Nuclear spin eigenvalues and eigenvectors in electron spin echo modulation, *in* "Electronic Magnetic Resonance of the Solid State" (J. A. Weil, Ed.), pp. 99–110. The Canadian Society for Chemistry, Ottawa (1987).
26. J. Mathews and R. L. Walker, "Mathematical Methods of Physics," Benjamin, Elmsford, New York (1965).
27. A. E. True, M. J. Nelson, R. A. Venters, W. H. Orme-Johnson, and B. M. Hoffman, *J. Am. Chem. Soc.* **110,** 1935–1943 (1988).
28. W. H. Orme-Johnson, *Ann. Rev. Biophys. Chem.* **14,** 419–459 (1985).
29. R. A. Venters, M. J. Nelson, P. A. McLean, A. E. True, M. A. Levy, B. M. Hoffman, and W. H. Orme-Johnson, *J. Am. Chem. Soc.* **108,** 3487–3498 (1986).
30. P. Kottis and R. Lefebvre, *J. Chem. Phys.* **39,** 393–403 (1963).
31. B. E. Sturgeon, P. E. Doan, K. E. Liu, D. Burdi, W. H. Tong, J. M. Nocek, N. Gupta, J. Stubbe, D. M. Kurtz, S. J. Lippard, and B. M. Hoffman, *J. Am. Chem. Soc.* **119,** 375–386 (1997).
32. B. M. Hoffman, *J. Phys. Chem.* **98,** 11657–11665 (1994).
33. B. M. Hoffman, B. E. Sturgeon, P. E. Doan, V. J. Derose, K. E. Liu, and S. J. Lippard, *J. Am. Chem. Soc.* **116,** 6023–6024 (1994).
34. P. E. Doan, H.-I. Lee, and B. M. Hoffman, Manuscript in preparation.
35. K. Fukui, H. OhyaNishiguchi, and H. Kamada, *Inorg. Chem.* **36,** 5518–5529 (1997).
36. E. A. C. Lucken, *in* "Nuclear Quadrupole Coupling Constants," pp. 217–247, Academic Press, New York (1969).
37. H. Thomann, M. Bernardo, W. E. Newton, and D. R. Dean, *Proc. Natl. Acad. Sci. USA* **88,** 6620–6623 (1991).
38. H. Thomann, T. V. Morgan, H. Jin, S. J. N. Burgmayer, R. E. Bare, and E. I. Stiefel, *J. Am. Chem. Soc.* **109,** 7913–7914 (1987).
39. K. E. Brigle, R. A. Setterquist, D. R. Dean, J. S. Cantwell, M. C. Weiss, and W. E. Newton, *Proc. Natl. Acad. Sci. USA* **84,** 7066–7069 (1987).
40. K. E. Brigle, M. C. Weiss, W. E. Newton, and D. R. Dean, *J. Bacteriol.* **169,** 1547–1553 (1987).
41. C.-H. Kim, W. E. Newton, and D. R. Dean, *Biochemistry* **35,** 2798–2808 (1995).
42. C. L. Fan, P. E. Doan, C. E. Davoust, and B. M. Hoffman, *J. Magn. Reson.* **98,** 62–72 (1992).
43. W. B. Mims, *J. Magn. Reson.* **59,** 291–306 (1984).
44. J. K. Shergill and R. Cammack, *Biochim. Biophys. Acta* **1185,** 35–42 (1994).
45. S. A. Dikanov, R. M. Davydov, L. Xun, and M. K. Bowman, *J. Magn. Reson. B* **112,** 289–294 (1996).
46. R. D. Britt, K. Sauer, M. P. Klein, D. B. Knaff, A. Kriauciunas, C. A. Yu, L. Yu, and R. Malkin, *Biochemistry* **30,** 1892–1901 (1991).
47. J. K. Shergill, C. L. Joannou, J. R. Mason, and R. Cammack, *Biochemistry* **34,** 16533–16542 (1995).
48. J. K. Shergill and R. Cammack, *Biochim. Biophys. Acta* **1185,** 43–49 (1994).
49. J. K. Shergill and R. Cammack, *J. Chem. Soc.-Faraday Trans.* **89,** 3685–3689 (1993).
50. R. Cammack, A. Chapman, J. McCracken, J. B. Cornelius, J. Peisach, and J. H. Weiner, *Biochim. Biophys. Acta* **956,** 307–312 (1988).
51. H. C. Lee, E. Scheuring, J. Peisach, and M. R. Chance, *J. Am. Chem. Soc.* **119,** 12201–12209 (1997).
52. T. L. Stemmler, B. E. Sturgeon, D. W. Randall, R. D. Britt, and J. E. PennerHahn, *J. Am. Chem. Soc.* **119,** 9215–9225 (1997).
53. Y. Deligiannakis, A. Boussac, H. Bottin, V. Perrier, O. Barzu, and A. M. Gilles, *Biochemistry* **36,** 9446–9452 (1997).
54. Y. Deligiannakis, A. Boussac, and A. W. Rutherford, *Biochemistry* **34,** 16030–16038 (1995).
55. K. Warncke, H. B. Brooks, H.-I. Lee, J. McCracken, V. L. Davidson, and G. T. Babcock, *J. Am. Chem. Soc.* **117,** 10063–10075 (1995).
56. H.-I. Lee, Ph. D. Thesis, Michigan State Univ., East Lansing (1994).
57. F. Jiang, J. McCracken, and J. Peisach, *J. Am. Chem. Soc.* **112,** 9035–9044 (1990).
58. J. McCracken, S. Pember, S. J. Benkovic, J. J. Villafranca, R. J. Miller, and J. Peisach, *J. Am. Chem. Soc.* **110,** 1069–1074 (1988).